INDONESIAN JOURNAL ON GEOSCIENCE
Geological Agency
Ministry of Energy and Mineral Resources

Journal homepage: http://ijog.geologi.esdm.go.id
ISSN 2355-9314, e-ISSN 2355-9306

Application of Landsat 8 Image in An Assessment of Hydrothermal Alteration Mapping in Dense Vegetation: A Case Study from Kokap Area, Kulon Progo

Agung Setianto[1], Bayu Raharja[1,2*], and Anastasia Dewi Titisari[1]

[1]Department of Geological Engineering, Gadjah Mada University (UGM)
Jln. Grafika No. 2, Yogyakarta, Indonesia. 55284
[2]Directorate General of Mineral and Coal, Ministry of Energy and Mineral Resources
Jln. Dr. Soepomo No.10, Tebet, Jakarta Selatan, Indonesia. 12870

Corresponding author: bayu.raharja@esdm.go.id
Manuscript received: December, 16, 2019; revised: November, 21, 2020;
approved: April 13, 2021; available online: December, 13, 2021

Abstract - Several researchers through geochemical analysis have proven the presence of gold mineralization in Kokap, Kulon Progo, as a result of hydrothermal alteration. Alteration mapping with optical remote sensing images in tropical areas is very difficult due to atmospheric conditions, dense vegetation cover, and rapid weathering. This study aims to assess the ability of Landsat 8 images in the mapping of hydrothermal alteration in Kokap, Kulon Progo, with the Principles Component Analysis (PCA) method. Three conventional machine learning methods, including artificial neural network (ANN), maximum likelihood classification (MLC), and support vector machine (SVM) were compared to find an optimal classifier for hydrothermal alteration mapping. The experiment revealed that the MLC method offered the highest overall accuracy. Two alteration zones were mapped, *i.e.* argillic zone and propylitic zone. The comparison results showed that the MLC classification of band ratio images of 5:2 and 6:7 yielded a classification accuracy of 56.4% and kappa coefficient of 0.36, which was higher than those of other machine learning methods and band combinations. The combination of Landsat 8 with DEM succeeded in increasing accuracy to 59.5% with kappa coefficient of 0.4.

Keywords: hydrothermal alteration, Landsat 8, principle component analysis, multispectral classification.

How to cite this article:
Setianto, A., Raharja, B., and Titisari, A.D., 2022. Application of Landsat 8 Image in An Assessment of Hydrothermal Alteration Mapping in Dense Vegetation: A Case Study from Kokap Area, Kulon Progo. *Indonesian Journal on Geoscience*, 9 (1), p.45-60. DOI: 10.17014/ijog.9.1.45-60

Introduction

Background

The utility of remotely sensed data in geological applications such as mineral potential and hydrothermal alteration mapping has shown a great success, especially in arid areas with low vegetation cover. The Landsat-8 satellite was launched by the National Aeronautics and Space Administration (NASA) in April 2013 as a part of the Landsat Data Continuity Mission (LDCM). It consists of two sensors: OLI (Operational and Imager) with a spectral range from visible (0.43−0.88 µm) to short wave (1.57 - 2.29 µm) and TIRS (Thermal Infrared Sensor) with thermal spectral range of 10.6 - 12.51 µm. Bedell (2001) used remotely sensed data, especially the visible band to map vegetation and identify iron-oxide minerals, also shortwave band to identify carbonate minerals and lithological types. Yamaguchi and Naito (2003) used the thermal band to identify silicate rocks.

Some aspects must be considered due to the use of remote sensing data for mineral exploration and hydrothermal mapping. First, the sensor facing interference while recording the earth surface as the effect from the atmosphere, cloud, and vegetation cover. Second, common methods such as band ratio and principle component do not quantitatively measure the abundance of minerals, but only showed the indication or anomalies that may reflect the presence of minerals. Hence, validation through field survey must be carried out. Finally, each location has its own characteristics, thus a method that succeeds in mapping out the mineralized zone in one location may probably not be successful when applied to the other location. It is important always to support the remote sensing analysis with other types of data such as geological and structure maps, geochemical, and geophysical data, *etc*.

Several researchers have proved that potential gold mineralization areas could be successfully detected as a result from hydrothermal alteration through geochemical analysis in Kokap, Kulon Progo (Harjanto, 2010; Nugraha, 2015; Sulthoni, 2017; Pambudi, 2017; and Pramumijoyo, 2017). At least, there were three hydrothermal alteration zones successfully mapped in the studied area: silicification, argillic, and propylitic zones. Each of these alteration zones has its own spectral signatures and can be identified through a remote sensing analysis. The aims of this paper are: (i) to perform principle analysis to map hydrothermal alteration zones, (ii) to validate the results based on field data; and (iii) to find which band combination and machine learning method performs best in mapping the distribution of alteration based on accuracy.

Geological/Stratigraphical Settings

The studied area is located in the western part of Kulon Progo Regency, Yogyakarta Special Region, with an area around 80 km^2. Bemmelen (1949) named the Kulon Progo Mountains as an oblong dome because of its elliptical shape morphology. This oblong dome shape was formed due to the uplift event composed of Oligo-Miocene old andesitic volcanic materials from Gajah, Ijo, and Menoreh Volcanoes. Gajah Volcano was firstly formed in the centre of Oblong Dome and produces basaltic andesite followed by Ijo Volcano in the southern part of the dome that produces andesite pyroxene and dacite intrusion. Finally, Menoreh Volcano formed in the northern part of the dome and produce andesite hornblende, dacite, and andesite intrusion (Suroso *et al*., 1986).

According to the Regional Geological Map number 1408-2 and 1407-5 from Geological Agency of Republic Indonesia (Figure 1), the studied area is located in the Oligo-Miocene andesite intrusion (a). This intrusion breaks through Nanggulan Formation (Teon) and Kebobutak Formation (Tmok) (Rahardjo *et al*., 1995). Some geological structures were identified as a result of volcanism and secondary processes (Widagdo *et al*., 2016). The hydrothermal fluid carrying mineralization was then circulated through this geological structure. These may be faults, joints, cracks, or fissures or simply boundaries of grains. (Pramumijoyo, 2017).

Hydrothermal alteration in the studied area has been grouped into three alteration zones with different mineral assembly character (Harjanto, 2010; Pramumijoyo, 2017, and Sulthoni, 2017). Silicification zone (highly altered) located in the centre of alteration is typically characterized by secondary minerals of quartz and illite. Argillic zone (medium altered) is typically characterized by the presence of illite, montmorillonite, and kaolinite. Propylitic alteration, the outermost zone formed in the lower temperature, typically contains chlorite and epidote as the secondary altered mineral.

Methods and Materials

Digital Image Processing

The image used in this study is the Landsat 8 image (path 120 row 65) recorded on September 18, 2015 with a 12-bit radiometric resolution. The visible near infrared (VNIR) and shortwave infrared (SWIR) bands were combined to form

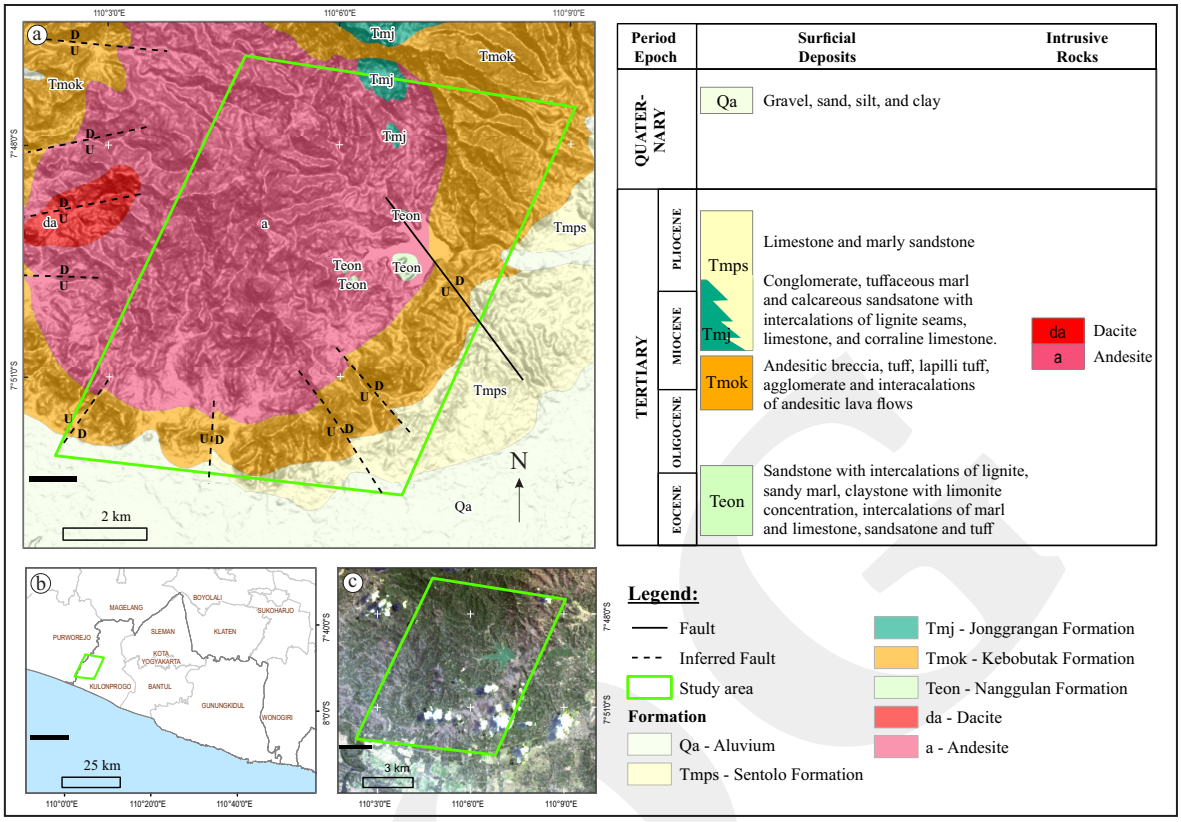

Figure 1. Geological map of Kokap and surrounding areas modified from Regional Geological Map created by Geological Agency of Republic Indonesia (A). Index map of Yogyakarta Special Region. Studied area (E110,0383°-110.1511° and S7,78103°-7,8671°) is marked with polygon in light green colour (B). Landsat 8 true colour composite image (RGB: bands 4-3-2) (C).

seven bands at 30 m spatial resolution. Thermal infrared bands (TIR) were not used in this study. This scene was geo-referenced in the UTM zone 49S coordinate system with WGS-84 ellipsoid, but has not been systematically radiometric corrected. This mean, the pixel value (digital number) needs to be calibrated. Furthermore, the value of the digital number (DN) was converted to the spectral radiance sensor to calibrate the sensor based on the coefficient in its metadata (Wicaksono and Danoedoro, 2012).

This spectral radiance value was then converted to Top of Atmospheric (TOA) reflectance and followed by atmospheric correction using FLAASH (Fast Line-of-sight Atmospheric Analysis of Hypercubes) method. Atmospheric correction aimed to eliminate the influence of elements and molecules in the atmosphere, resulted surface reflectance value (Vermote *et al.*, 2002). Masking process was then performed to crop the image only at the studied area and eliminate other objects such as the sea and clouds, since it would interfere with the PC processes. The statistical value of the Landsat 8 image after masking process can be seen in Table 1.

Table 1. Landsat 8 Band 1-7 Statistic After Masking (digital number is in reflectance)

Band	Min	Max	Mean	Stdev
Band 1	0.0	0.559	0.027	0.036
Band 2	0.0	0.593	0.029	0.037
Band 3	0.0	0.650	0.042	0.045
Band 4	0.0	0.693	0.038	0.045
Band 5	0.0	0.810	0.163	0.139
Band 6	0.0	0.782	0.109	0.099
Band 7	0.0	0.628	0.058	0.059

Remote Sensing for Mineral Identification

The approach used to map hydrothermal alterations from satellite imagery in this study is to identify the mineral assembly of hydrothermal

alteration such as quartz, kaolinite, epidote, illite, chlorite, montmorillonite, sericite, and other clay minerals. Visible and shortwave band of Landsat 8 image were considered as bands that can be used to distinguish the type of mineral from its spectral reflection characteristics or spectral signature. Based on this spectral characteristic, an algorithm can be arranged to highlight target minerals and minimize the spectral response of other objects (Figure 2). Some algorithms that are often used are band ratio and principle component analysis (Abrams *et al*., 1977; Taranik and Crosta, 1996; Carranza, 2002). For example, chlorite has a high spectral reflectance on Landsat 8 band 7 and a low spectral reflectance on Landsat 8 band 2. One of the common problems encountered in the mineral mapping in areas with dense vegetation is how to distinguish the responses of these two elements. Both vegetation and minerals have good response in the infrared wavelengths.

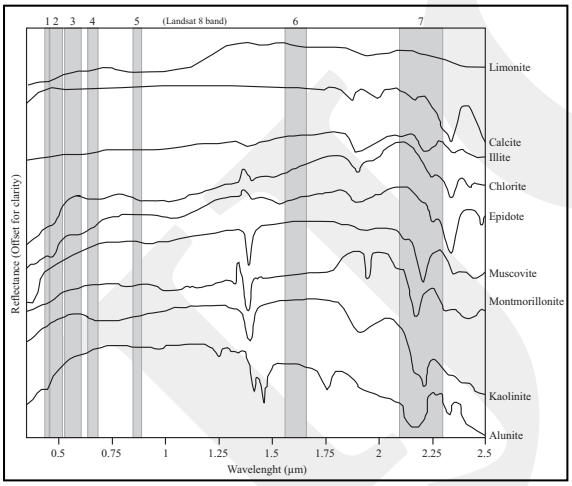

Figure 2. Laboratory reflectance spectra of some important alteration minerals (Livo *et al*., 1993).

Principle Component Analysis (PCA)

PCA is a process of transforming spectral values on images with the aim of reducing the data redundancy. The results of PCA transformation called PC bands that contain bands that do not correlate one with another. PC1 can contain data with the largest percentage variance, PC2 contains the second largest percentage variance *etc.* until the last PC which contain only noise (Murti and Wicaksono 2014; Gasmi *et al.*, 2016). The input of PCA is the statistical data from an image such as mean, standard deviation, variance, covariance, and correlation from each band. These statistics will then be arranged into a matrix that is used to get the eigen vector and eigen values to rotate the original data (Murti and Wicaksono, 2014; Smith, 2005).

This technique has successfully been applied by researchers in various locations to map hydrothermal alteration (Davidson *et al*., 1993; Ruiz-Armenta and Prol-Ledesma 1998; Souza Filho and Drury, 1998; Tangestani and Moore 2002; Crosta *et al*., 2003). Two different input of Landsat 8 bands were used as PC input in this study. First, a combination of three or four Landsat 8 bands which has high and low spectral respond on target mineral and vegetation (also known as PCA or Crósta method). Second, a combination of two-band ratio images (also known as direct principle component or DPC or software defoliant technique). First band ratio image should highlight the target mineral, and the second band ratio should contain information about another object that interfering the target mineral (*i.e.* vegetation) (Fraser and Green, 1987; Carranza, 2002). When there were only two bands used as input to PC processes, the spectral contrast was mapped into the second component. By limiting the number of PC input, it is expected that the result will be easier for visual interpretation.

Band selection as PC input was based on the spectral response of Landsat 8 bands to each target minerals (Table 2). The matrix used in PC calculations is the covariance matrix. The results of

Table 2. Landsat 8 Bands Combination for PC

Target	PC combination	DPC combination
Illite	3-5-7	5/3; 7/2
Kaolinite + montmorillonite	3-6-7	5/4; 6/7
Epidote	2-6-7	5/2; 6/7
Chlorite	2-3-6	5/3; 6/2
Quartz	2-4-7	3/4; 7/2
Limonitic alteration zone	2-4-5-6	4/2; 5/4
Clay alteration zone	2-5-6-7	5/4; 6/7

PCs showed the areas containing targeted mineral usually exhibit high eigen vector loading value. If the loading of the reflective band is positive in sign, the target area is shown by bright pixels. If the loading of the reflective band is negative, the area is shown by dark pixels. In contrast, if the loading of the absorptive band is positive in sign, the target area is shown by dark pixels. If the loading of the absorptive band is negative, the area is shown by bright pixels (Crosta and Moore, 1989).

Multispectral Classification

One common way to group pixels or digital number from an image with similar characteristic is to use the Per-Pixel Analysis (PPA) technique or often called Per-Pixel Classification. This method assumes that each object on the surface of the earth has a different spectral reflectance so that it can be grouped based on its spectral value. This classification can be divided into supervised and unsupervised classifications (Richards, 1999; Danoedoro, 2012). This study used the supervised classification with three different machine learning methods, *i.e.* artificial neural network (ANN), maximum likelihood classification (MLC), and support vector machine (SVM). A brief explanation of these three algorithms were provided in Lehmann and Casella, (1998), Haykin (2004), Mondal *et al*. (2012), Wang *et al*. (2017), Ge *et al*. (2018), and were not repeated here.

Confusion matrix (or classification error matrix) was then performed to quantitatively measure multispectral classification accuracy. Confusion matrix contains statistical information such as overall accuracy, kappa analysis, and the Z-statistic that useful to find out whether a classification is successful or failed. Kappa analysis is a discrete multivariate technique used in the accuracy assessment to statistically determine whether one error matrix is significantly different from other matrices (Bishop *et al*., 1975). The minimum overall acceptable level of accuracy is 85% (Anderson *et al*., 1976) with kappa values greater than 0.8 which means having a high level of conformity (Congalton and Green, 1999; Carranza, 2002).

Result

Landsat 8 Principle Component Analysis

Several combinations of PC inputs were carried out to obtain the distribution of the secondary altered minerals such as kaolinite, montmorillonite, illite, clay alteration, and limonitic alteration. The combination of Landsat 8 bands 3-6-7 was used to identify the abundant of kaolinite and montmorillonite. Both minerals have a high spectral response on band 3 and band 6, and have low reflectance on band 7. The PC results show that PC1 has positive loadings for all output bands. PC2 has high and opposite eigen vector loadings for band 3 (0.84) and band 7 (-0.50). The value of this loadings is higher than the value of eigen vector loadings on PC3 for band 6 (- 0.20) and band 7 (0.86). Thus, the PC2 was chosen to display the abundance of kaolinite and montmorillonite minerals containing 0.64% of the total variance in the spectral data.

A combination of Landsat 8 bands 3-5-7 was used to map illite. Illite has a high spectral response in Landsat 8 band 3 and band 5, and has a low response on band 7. The PC results show that PC1 has positive eigen vector loadings for all band. PC2 has high and negative eigen vector loadings on band 5 (-0.79) and negative eigen vector loading on band 7 (-0.23). PC3 has the same positive loadings value for band 3 and band 5 (0.58), and has negative loadings for band 7 (-0.57). Illite is explained in PC3 as bright pixel which contain 1.34% of the total variance in the spectral data.

To target clay alteration, a combination of bands 2-5-6-7 is used as an input to the PC. The result shows that PC1 has positive loadings for all band representing albedo and topographic information. PC2 representing the vegetation response has a high and negative loading on band 5 (-0.80). PC3 has a contrast loading value between VNIR and SWIR band, with the value of -0.77 on band 7 (SWIR) and 0.51 on band 2 (VNIR). PC4 was chosen to display the clay alteration, because it has a high and opposite eigen vector loading on band 6 (-0.54) and band 7 (0.60) in the output PC

image. Clay alteration displays in bright pixel because of the high positive eigen vector loading value from band 7. PC4 contains less than 1% of the total variance in the spectral data.

Limonitic alteration was mapped using a combination of bands 2-4-5-6 that sensitive to map ferric ion elements. The best PC results were given by PC3 with the contrast loading value between band 2 (0.48) and band 4 (-0.78). The negative loading value from band 4 indicates that the abundance of limonitic alteration will be mapped as dark pixel. To display limonitic alteration in bright pixel, PC3 must be negated. PC3 contains 0.96% of the total variance in the spectral data.

The selected PC results with loadings in bold indicates the target minerals (Table 3). PC images show that the abundance of kaolinite and montmorillonite (Figure 3a), illite(Figure 3b), clay alteration (Figure 3c), and limonitic alteration (Figure 3d) is associated with sparse vegetation in NDVI images (Figure 3e). On the other hand, the known hydrothermal alteration zones carrying mineralization (polygon with magenta lines in Figure 3f) are in the densely vegetation area in which PC images failed to map this.

Landsat 8 Directed Principal Component Analysis

Quartz was mapped using band ratio images 4:3 (sensitive to vegetation) and band 7:2 (to map quart). DPC analysis with band ratio images 3:4 and 6:2 was used to map montmorillonite based on the spectral characteristic of montmorillonite (high reflectance in band 6 and low reflectance in band 2). Illite has a high spectral response on band 7 and low spectral response on band 2. The combination of ratio images 5:3 and 7: 2 was then chosen to map the abundance of illite. Chlorite is best mapped with band ratio image 6:2, because they have a high spectral response on band 6 and a low spectral response on band 2. To separate vegetation from chlorite, combination of band ratio image 5:3 was selected. Thus, chlorite was mapped with band ratio image of 6:2 and 5:3. Epidote was mapped using a combination of band ratio 5:2 (good for vegetation identification) and band ratio image 6:7 (best to map epidote).

The results show that all DPC calculations have strong similarity based on loadings value (both negative value) in DPC1, so that vegeta-

Table 3. Eigenvector Loadings for Landsat 8 PCA Combination

	PC1	PC2	PC3	PC4	Alteration minerals
Band 3	0.29	**0.84**	0.46	-	Kaolinite + montmorillonite
Band 6	0.95	-0.22	-0.20	-	
Band 7	0.06	**-0.50**	0.86	-	
Eigen values (%)	98.90	**0.64**	0.46	-	
Band 3	0.59	0.57	0.58	-	Illite
Band 5	0.19	**-0.79**	0.58	-	
Band 7	0.79	**0.23**	-0.57	-	
Eigen values (%)	93.76	**4.90**	1.34	-	
Band 2	0.50	0.48	0.51	0.51	Clay alteration
Band 5	0.52	-0.80	-0.03	0.29	
Band 6	0.70	0.27	-0.38	**-0.54**	
Band 7	-0.04	0.23	-0.77	**0.60**	
Eigen values (%)	93.38	4.89	1.66	**0.07**	
Band 2	0.50	0.51	**0.48**	0.51	Limonitic alteration
Band 4	0.47	0.39	**-0.78**	-0.11	
Band 5	0.56	-0.17	0.36	-0.72	
Band 6	0.46	-0.75	-0.16	0.45	
Eigen values (%)	93.31	5.50	**0.96**	0.24	

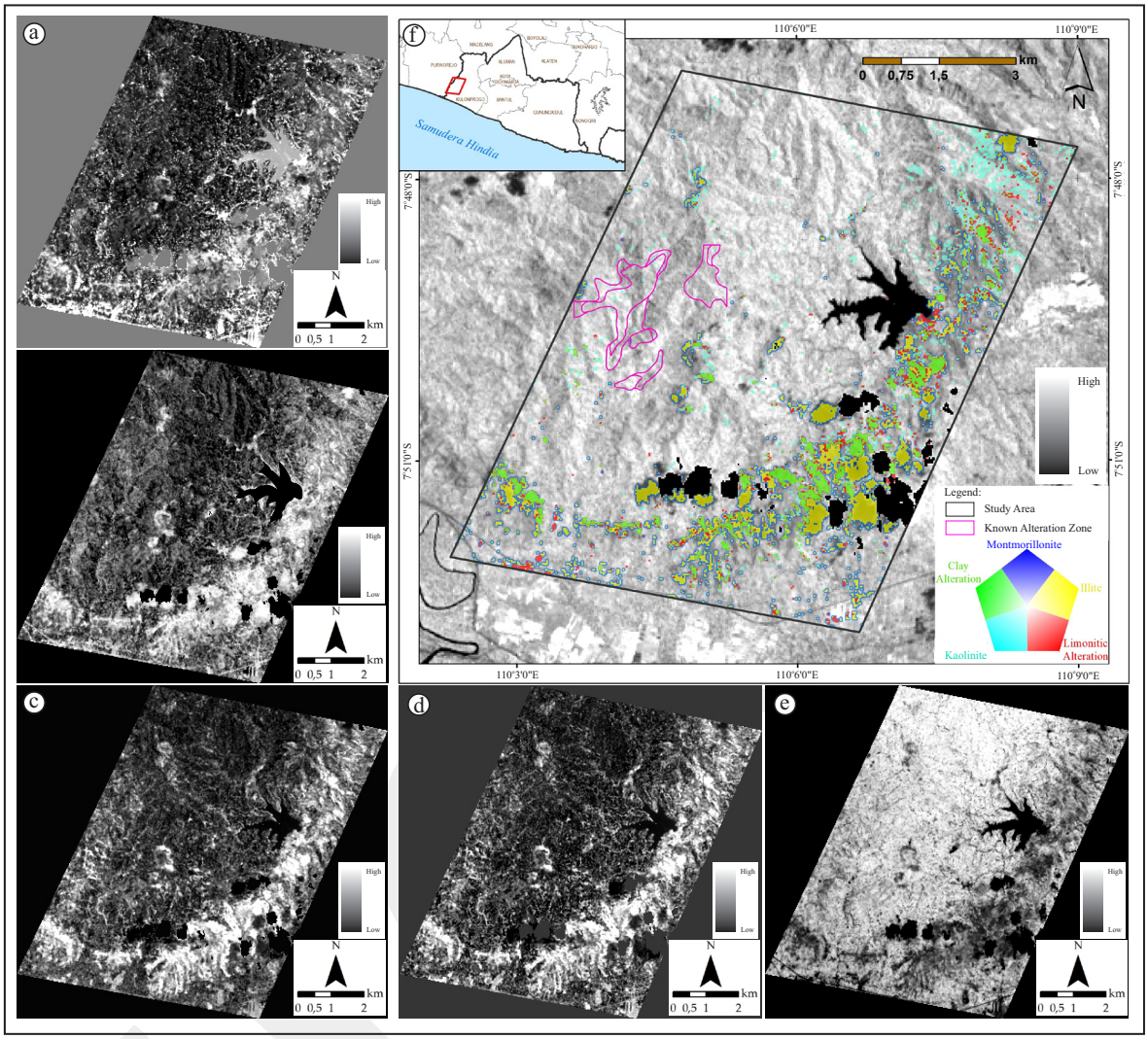

Figure 3. PCA images show the abundance of kaolinite and montmorillonite (a), illite (b), clay alteration (c) limonitic alteration (d) and NDVI (e). Abundant minerals with confidence threshold 95% are displayed as different colour and draped over Landsat 8 band 5 (f). Pixel brightness in mineral images (a-d) indicates the relative abundance of mineral considered. Pixel bright in NDVI images (e) indicates densely vegetation. Polygon in magenta lines (f) are known alteration zones mapped by Pramumijoyo (2017). The abundance of alteration minerals located outside of known alteration zones.

tion and target minerals cannot be differentiated. DPC2 has opposite loading value sign (positive and negative) thus map zones containing target minerals. All target minerals in DPC2 will be displayed as bright pixels. The DPC2 component for each alteration minerals were account less than 3% of the total variance in the spectral data. Target minerals in the selected DPC are characterized by eigen vector loadings in bold (Table 4) and mapped as bright pixels in the DPC images (Figure 4a-e). DPC image shows that the abundance of altered minerals is associated with sparse vegetation in NDVI images (Figure 4f). DPC seems to be failed to map the known alteration zones since it is not overlapping with the abundance of altered minerals (bright pixels).

According to PC results (Figures 3 and 4), most of the dense vegetation areas were mapped as dark pixels in the PC images. This is probably because vegetation density interfered spectral responses of target mineral, hence only digital number from vegetation is processed by PC. It is also possible that the presence of target minerals is not in a large abundance. The spatial resolution used in this study is 30 m. This means, if mineral

Table 4. Eigenvector Loadings for Landsat 8 DPC Combination

	DPC1	DPC2	Alteration minerals
Band 3 : Band 4	-0.42	**-0.91**	
Band 7 : Band 2	-0.91	**0.42**	Quartz
Eigen values (%)	97.02	**2.98**	
Band 3 : Band 4	-0.23	**-0.97**	
Band 6 : Band 2	-0.97	**0.23**	Montmorillonite
Eigen values (%)	99.15	**0.85**	
Band 5 : Band 3	-0.90	**-0.44**	
Band 7 : Band 2	-0.44	**0.90**	Illite
Eigen values (%)	97.67	**2.33**	
Band 5 : Band 3	-0.70	**-0.71**	
Band 6 : Band 2	-0.71	**0.70**	Chlorite
Eigen values (%)	98.36	**1.64**	
Band 5 : Band 2	-0.98	**-0.21**	
Band 6 : Band 7	-0.21	**0.98**	Epidote
Eigen values (%)	99.10	**0.90**	

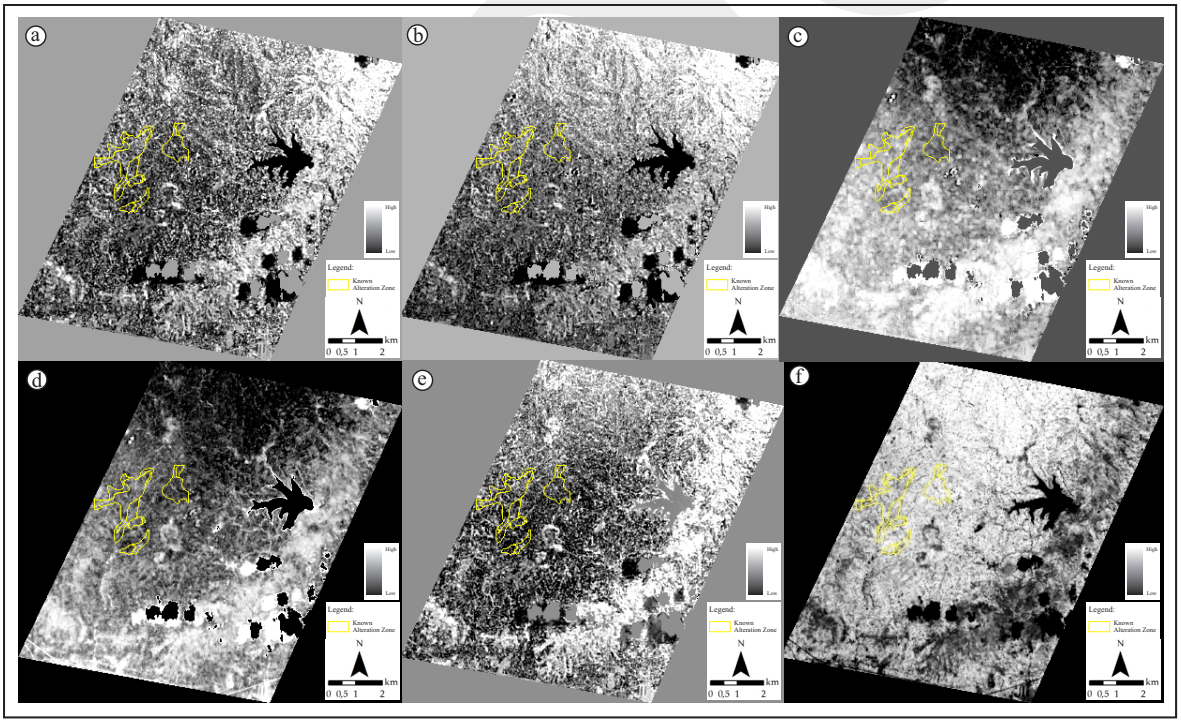

Figure 4. Abundant mineral images for quartz (a), montmorillonite (b), epidote (c), illite (d), and chlorite (e) produced using DPC of Landsat 8 bands. Pixel brightness in mineral images (a-e) indicates relative abundance of mineral considered. Pixel bright in NDVI images (f) indicates densely vegetation. Polygon in yellow lines are known alteration zones mapped by Pramumijoyo (2017).

is present insufficient abundant, PC cannot map it. Since PC was failed to map hydrothermal alteration in the studied area, other approaches with multispectral classification need to be done.

Multispectral Classification

PC images generated from Landsat 8 band was then classified into hydrothermal alteration zones by ANN, MLC, and SVM classification based on

the primary observation data and secondary data collections (Harjanto, 2010; Sulthoni, 2017; and Pramumijoyo, 2017). These data (Figure 5a) were divided into two sets of pixels used for supervised

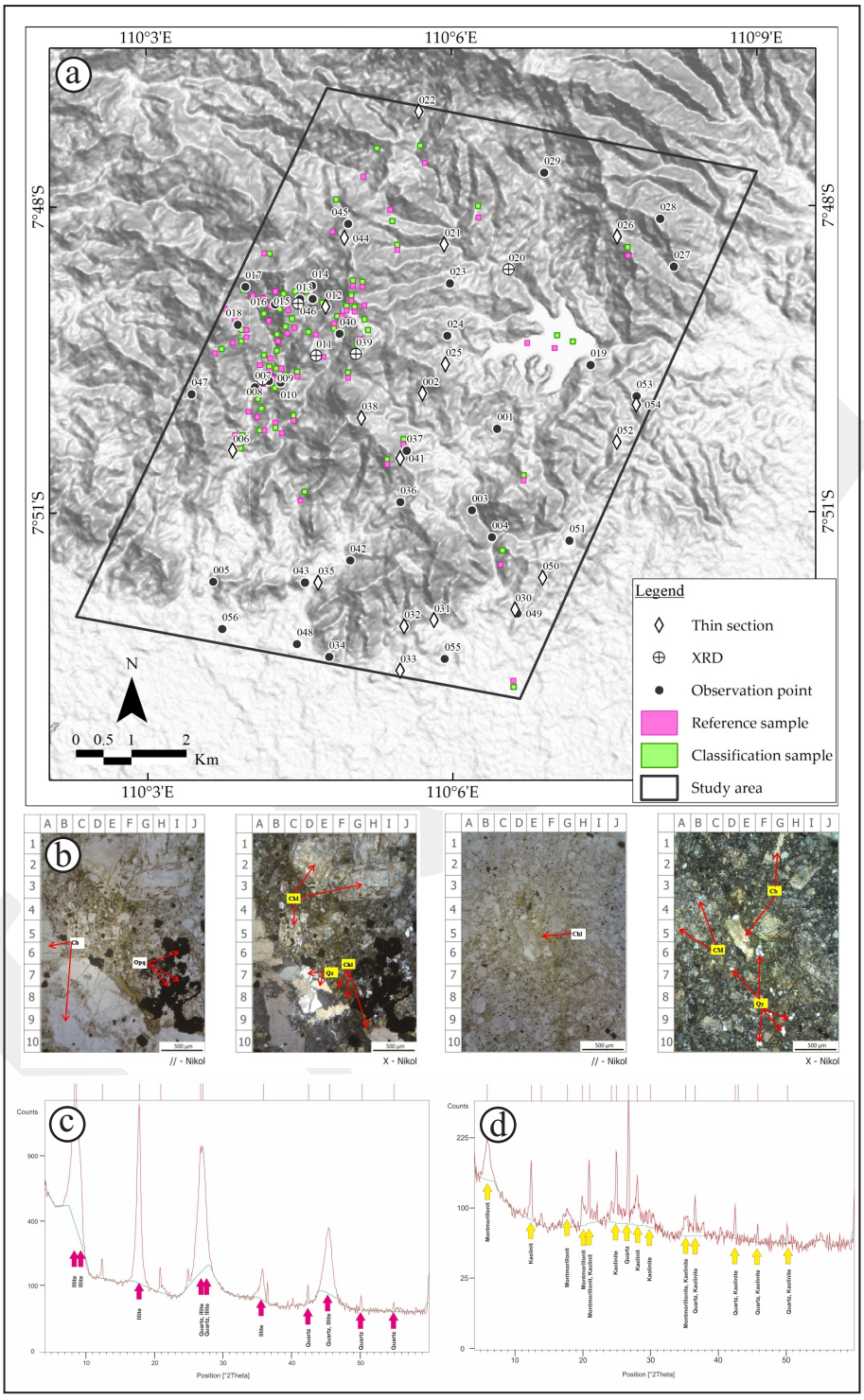

Figure 5. Distribution of thin section location (diamond), XRD locations (circle), observation point (black dot), training pixels (green square), and testing pixels (pink square) in the studied area (a). Thin section analysis from sample 012 showed an altered rock. It is originally an igneous rock with porphyritic texture. Minerals consist of carbonate/Cb (40%), secondary quartz/Qz (10%), clay minerals/Cm (15%), chlorite/Chl (30%), and opaque minerals/Opx (5%) indicated as propylitic alteration (b). Some alteration minerals detected from sample 020 (c) and 039 (d) by XRD analysis include quartz, illite, kaolinite, and montmorillonite. This location is experienced silicification (sample 020) and argillic (sample 039) alteration.

classification: (a) training pixels (classification sample) and (b) testing pixels (reference sample). The selected observation sites obtained from each set were collected and subjected to X-ray diffraction (XRD) analysis (Figure 5b) and observations of thin sections under a microscope (Figure 5c). Some minerals such as quartz, kaolinite, illite, and montmorillonite were present (Table 5). Alteration zones were identified as silicification, argillic, and propylitic based on the mineral assemblies. Although three types of alteration zones have been identified, only two alteration zones can be mapped in this study because of Landsat 8 spatial resolution limitation. These units are, respectively, the argillic and propylitic zones. Silicification was excluded from the computation because of its low abundant and not being captured by Landsat 8 image. Training and testing pixels also contain information about the water body and unaltered area.

The supervised classification was performed to map the hydrothermal alteration zone based on PC images and sample data. The classification accuracies and kappa coefficients of hydrothermal alteration mapping results of Landsat 8 using different machine learning methods are displayed in Table 6. The experiment revealed that the MLC method offered the highest overall accuracy compared to ANN and SVM methods.

Highest classification result showed by the MLC method with an input of Landsat 8 image ratios of 5:2 and 6:7. This combination yielded overall a classification accuracy of 56.64%, kappa coefficient of 0.36 and Z-statistic value of 17.93 (Figure 6a). Z-statistic value is exceeding the critical value at 95% confidence level, implies that this classification is better than random classification. ALOS Palsar DEM was then used together with PC images to improve the accuracy of hydrothermal alteration classification. DEM value which lay from 32 m to 622 m was stretched to 0 - 1 scale, similar to the ranges of another images. This combination succeeded in increasing the overall accuracy to 59.5% with a kappa coefficient of 0.4 and Z-statistic value of 20.35. Notice that the argillic zones decrease, followed by the increasing of unaltered zones (Figure 6b). The best Landsat 8 band combination for multispectral classification is marked in bold text in Table 6.

Pairwise comparison (Table 6) is used to compare the error matrices, two at a time, to determine if they are significantly different. It shows that these two matrices (both before and after the use of ALOS Palsar DEM) are not significantly different. Notice the pairwise comparison value is commonly less than the critical value (at 95% confidence level, the critical value would be 1.96). This is not surprising, because the differences between overall accuracies and the kappa coefficients before and after DEM are not significantly different, respectively.

Comparison hydrothermal alteration zone mapping between multispectral classification and the known hydrothermal alteration zones are presented in Figure 6c and d. These known alteration zones were mapped by Pramumijoyo (2017) and Harjanto (2010) with field observation followed by geochemistry analysis. Basically, it is a comparison between geochemistry analysis and

Table 5. Rock Samples Representing Altered Minerals

Sample Number	Analysis	Altered minerals	Altered Zone
008; 011; 015	XRD	Quartz Illite	Silicification
020; 039	XRD	Illite Montmorillonite Kaolinite	Argillic
006; 012; 021; 025	Thin Section	Chlorite, Carbonate	Propylitic

Table 6. Accuracy Assessment of Landsat 8 Multispectral Classification

Method	Band combination	Before ALOS Palsar DEM			After ALOS Palsar DEM			Pairwise
		Overall accuracy	Kappa	Z	Overall accuracy	Kappa	Z	comparison
MLC	PCA 3-5-7	51.57%	0.28	13.86	54.37%	0.32	16.11	1.54
	PCA 3-6-7	51.41%	0.28	13.83	55.09%	0.33	16.68	1.98
	PCA 2-5-6-7	54.55%	0.32	16.39	57.58%	0.37	18.70	1.62
	PCA 2-4-5-6	52.61%	0.29	14.88	57.34%	0.37	18.49	2.52
	DPC b3/b4-b7/b2	54.63%	0.33	16.50	57.10%	0.36	18.53	1.37
	DPC b3/b4-b6/b2	53.26%	0.31	15.42	54.85%	0.33	16.86	1.51
	DPC b5/b3-b7/b2	56.15%	0.35	17.73	58.94%	0.39	19.92	1.85
	DPC b5/b3-b6/b2	54.87%	0.33	16.62	58.22%	0.38	19.35	1.61
	DPC b5/b2-b6/b7	**56.64%**	**0.36**	**17.93**	**59.50%**	**0.40**	**20.35**	**1.50**
	DPC b5/b4-b6/b7	53.10%	0.30	15.33	53.97%	0.32	16.11	1.67
	DPC b4/b2-b5/b4	55.67%	0.34	17.21	58.62%	0.39	19.72	1.54
ANN	PCA 3-5-7	46.77%	0.20	8.59	54.55%	0.19	6.94	0.04
	PCA 3-6-7	46.06%	0.15	6.21	57.88%	0.26	9.27	2.93
	PCA 2-5-6-7	50.09%	0.29	13.83	56.71%	0.35	10.69	1.67
	PCA 2-4-5-6	48.08%	0.23	10.24	57.39%	0.29	10.38	1.68
	DPC b3/b4-b7/b2	43.64%	0.11	4.47	51.21%	0.31	3.02	0.50
	DPC b3/b4-b6/b2	45.45%	0.19	8.70	51.92%	0.24	9.97	1.50
	DPC b5/b3-b7/b2	51.68%	0.29	10.90	58.91%	0.36	14.25	2.03
	DPC b5/b3-b6/b2	46.67%	0.20	8.61	54.24%	0.25	9.91	1.65
	DPC b5/b2-b6/b7	50.40%	0.25	10.84	55.66%	0.28	10.98	0.86
	DPC b5/b4-b6/b7	51.92%	0.21	8.39	56.77%	0.25	9.09	0.95
	DPC b4/b2-b5/b4	48.18%	0.21	9.14	52.83%	0.24	9.50	0.80
SVM	PCA 3-5-7	53.03%	0.13	4.26	56.26%	0.33	9.54	3.24
	PCA 3-6-7	53.55%	0.20	7.15	55.96%	0.30	9.59	1.33
	PCA 2-5-6-7	54.45%	0.24	8.81	55.56%	0.27	9.32	0.27
	PCA 2-4-5-6	54.69%	0.26	9.70	56.17%	0.26	9.92	0.07
	DPC b3/b4-b7/b2	51.72%	0.10	3.33	55.56%	0.23	8.70	3.40
	DPC b3/b4-b6/b2	52.12%	0.12	4.05	55.76%	0.25	9.60	3.43
	DPC b5/b3-b7/b2	54.75%	0.22	7.92	56.78%	0.30	11.30	2.09
	DPC b5/b3-b6/b2	54.37%	0.26	9.31	56.89%	0.32	12.26	1.62
	DPC b5/b2-b6/b7	55.07%	0.29	11.33	58.01%	0.35	13.72	1.73
	DPC b5/b4-b6/b7	54.88%	0.26	10.74	56.98%	0.29	11.11	0.16
	DPC b4/b2-b5/b4	53.33%	0.19	6.83	57.58%	0.33	10.65	2.49

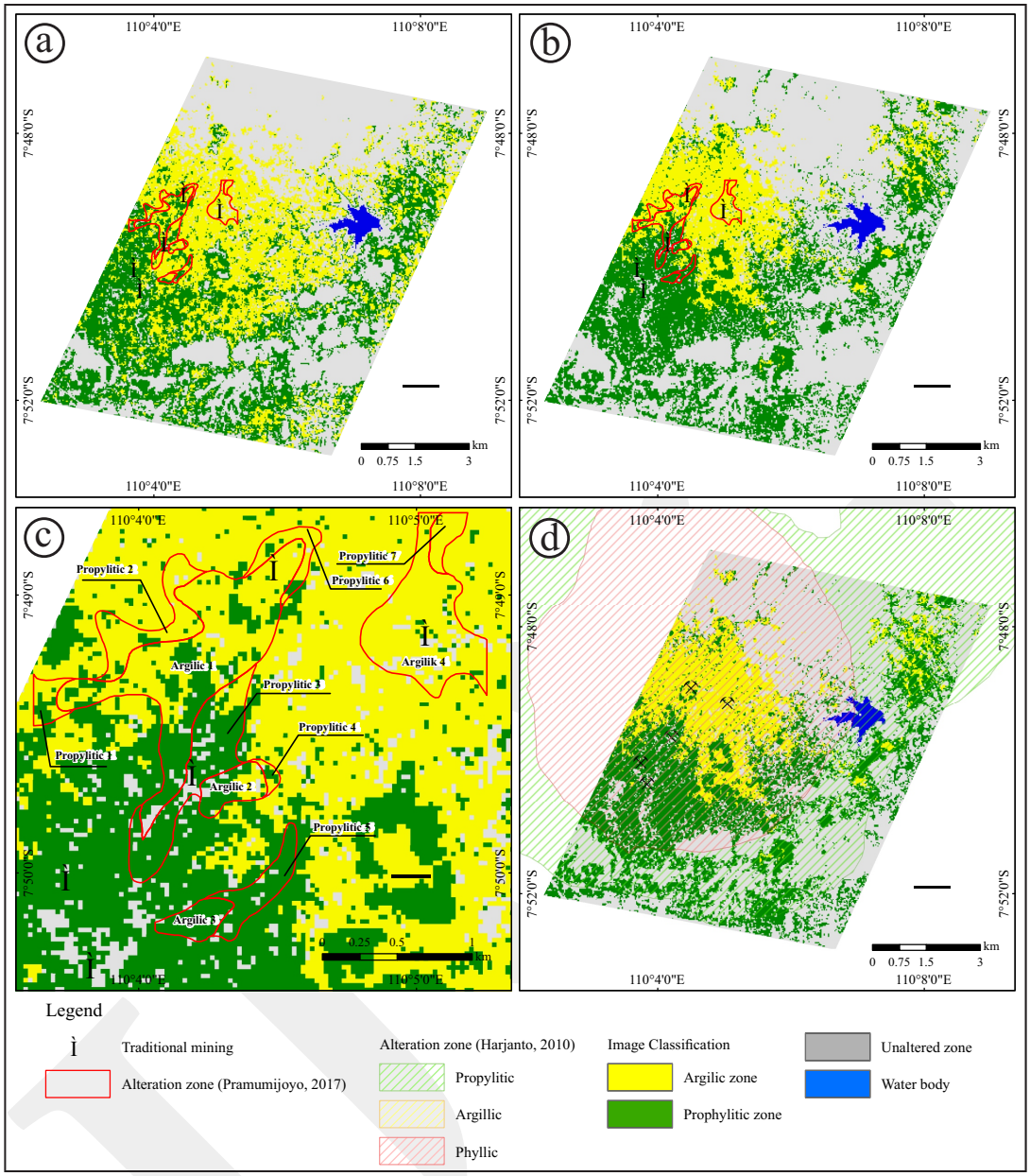

Figure 6. Hydrothermal alteration classification map from ratio images of 5:2 and 6:7 before combination with ALOS Palsar DEM (a) and after combination with ALOS Palsar DEM (b). DEM succeed in decreasing the argillic zones and increasing unaltered zones proven by the increasing value of overall accuracy and KHAT statistic which has higher agreement. Comparison of classified hydrothermal alteration zone derived from Landsat 8 image and field observation done by Pramumijoyo (2017) (c) and Harjanto (2010) (d) showed poor agreement for both argillic and propylitic zones. Some traditional mining location were also given in map to provide more information related to gold mineralization, respectively.

remote sensed method. Known alteration zones by Pramumijoyo (2017) were delineated into eleven hydrothermal alteration zone boundaries that consisted of seven propylitic zones and four argillic zones (Figure 6C). The result showed that multispectral classification tends to succeed to map hydrothermal alteration in zones of Propylitic 1, Propylitic 3, Propylitic 4, Propylitic 5, Argillic 1 and Argillic 4, and tend to be failed in zones of Propylitic 2, Propylitic 6, Propylitic 7, Argillic 2, and Argillic 3. Overall accuracy from this extent is about 50%, close to the overall accuracy for the whole studied area. Comparison between hydrothermal alteration classification and known alteration zones by Harjanto (2010) also showed poor agreement. Harjanto (2010)

divided the hydrothermal alteration as phyllic and propylitic zones according to its characterized mineral, while this research grouped the hydrothermal alteration as argillic and propylitic zones. Notice the location of phyllic zone mapped by Harjanto (2010) was overlapped with the argillic zone mapped by image classification (Figure 6d).

Discussion

In general, hydrothermal alteration mapping in this study is unsuccessful due to the value of overall accuracy and kappa coefficient that below the acceptance standard. This poor and unacceptable classification results occur because of the misclassification between argillic and propylitic zones. It is caused by some aspects, *i.e.* densely vegetation and spatial and spectral resolution of Landsat 8 image. More than two decades researchers agreed that mapping hydrothermal alteration zone in the dense vegetation using optical remote sensed data is indeed difficult since the vegetation digital number interfered mineral digital number. However, the DPC is proven more successful in the mineral detection mapping, compared to the PCA in this studied area.

Another factor that becomes very critical aspect is the spatial and spectral resolution of Landsat 8 data. Landsat 8 has 30 m spatial resolution which is categorized as medium resolution satellite data. This means, one-pixel Landsat 8 data, which is similar to 30 m x 30 m area, probably contain many objects on the earth surface. It is due to the digital number in one pixel of Landsat 8 image is not a purely digital number of one object entirely, but contains the digital number of different materials. The multispectral classification with Landsat 8 image only succeeds if the mapping target is in widely abundant, more than 30 m x 30 m. From spectral resolution point of view, Landsat 8 only has two SWIR bands which lay from 1.57 to 1.65 μm and from 2.11 to 2.29 μm. This spectral resolution availability makes Landsat 8 has limitation in the mineral and other geological object mapping. As mentioned in the previous chapter, the best band combination to map mineral, lithology, and other geological aspects is in the SWIR region. If SWIR band is available in many band ranges (for instance six bands in ASTER images), then many combinations of PC images can be created that may help in mineral detection and mapping.

However, despite the multispectral classification result is unacceptable, this study provides information about detailed hydrothermal alteration mapping accuracy that can be achieved using Landsat 8 image and DEM, especially in the dense vegetation cover. In the future, this method needs to be improved to increase the accuracy. It is true that remote sensing at high spatial and spectral resolution is essential, but the method that can highlight minerals in the dense vegetation is more important. From the exploration point of view, the utilization of Landsat 8 images in the mapping of hydrothermal alteration is very worthwhile since it is low-cost processing and promising result.

Conclusions

In this work, the potentials of principal component analysis (PCA) have been studied for hydrothermal alteration mapping using Landsat 8 images, especially the VNIR and SWIR bands. In the first place, image pre-processing including systematic radiometric correction and masking has been applied on seven Landsat 8 bands. In the second place, PCA is conducted to map the hydrothermal alteration with two different band combinations as input (also called PC and DPC). The analysis of PC images showed that the dense vegetation cover in the studied area obstructed the sensor penetration to the soil (or ground). It affects the unsuccessful result of mineral and hydrothermal alteration mapping. In the third place, field observation and geochemistry analysis are conducted to map the known hydrothermal alteration zones. The data will be used as training and test sample in multispectral classification processes. Finally, the multispectral classification with three

conventional machine learning methods: ANN, MLC, and SVM are conducted to determine the hydrothermal alteration zones using PC images and training and test data sample. The best overall accuracy is given by the MLC method using a combination of Landsat 8 images ratio of 5:2 and 6:7 with an accuracy of 56.64%, kappa coefficient of 0.36 and Z-statistic of 17.93. The combination of DEM with PC images increases the overall accuracy to 59.5% with kappa coefficient of 0.4 and Z-statistic of 20.35.

Acknowledgments

The authors would like to thank the Department of Geological Engineering, Gadjah Mada University, for their partly research funding, granted to the second author and fellow academic colleagues for material assistance and guidance provided for the completion of this work.

References

Abrams, M.J., Ashley, R.P., Rowan, L.C., Goetz, A.F.H., and Kahle, A.B., 1977. Mapping of hydrothermal alteration in the Cuprite mining district, Nevada, using aircraft scanner images for spectral region 0.46-2.36 mm. *Geology,* 5, p.713-718. DOI:10.1130/0091-7613(1977)5<713:mohait>2.0.co;2

Anderson, J.R., Hardy, E.E., Roach, J.T., and Witner, R.E., 1976. A land use and land cover classification system for use with remote sensor data. *USGS Professional Paper,* 964. DOI: 10.3133/pp964

Bedell, R.L., 2001. Geological mapping with ASTER satellite: new global satellite data that is a significant leap in remote sensing geologic and alteration mapping. *Special Publication, 33. Geological. Society of Nevada*, p.329-334.

Bemmelen, R.W. Van, 1949. *The Geology of Indonesia*, The Hague, Netherland,732pp.

Bishop, M.M., Feinberg, S.E., and Holland, P.W., 1975. *Discrete Multivariate Analysis: Theory and Practice.* MIT Press, Cambridge, Massachusetts, 587pp.

Carranza, E.J.M., 2002. *Geologically- constrained Mineral Potential Mapping*. Ph.D. Thesis, *Delft University of Technology*, The Netherlands, 480pp.

Congalton, R.G. and Green, K., 1999. *Assessing the Accuracy of Remotely Sensed Data: Principles and Practices*. Lewis Publishers, Boca Raton, FL, 137pp. DOI: 10.1201/9781420055139

Crósta, A.P. and Moore, J.M., 1989, Enhancement of Landsat Thematic Mapper imagery for residual soil mapping in SW Minas Gerias State, Brazil: a prospecting case history in Greenstone belt terrain. *Proceedings of the 7th Thematic Conference on Remote Sensing for Exploration Geology, Calgary*. p.1173-1187.

Crosta, A.P., Souza Filho, C.R., Azevedo, F., and Brodie, C., 2003. Targeting key alteration minerals in epithermal deposits in Patagonia, Argentina, Using ASTER imagery and principal component analysis, *International Journal of Remote sensing,* 24, p.4233-4240. DOI: 10.1109/igarss.1988.570231

Danoedoro, P., 2012. *Pengantar Penginderaan Jauh Digital*, Yogyakarta: Universitas Gadjah Mada.

Davidson, D., Bruce, B., and Jones, D., 1993. Operational remote sensing mineral exploration in a semi-arid environment: the Troodos Massif, Cyprus. *Proceedings of the 9th Thematic Conference on Remote Sensing for Exploration Geology, Pasadena*, CA (Ann Arbor, MI: Environmental Research Institute of Michigan), p.845-859. DOI: 10.22215/etd/1993-02478

Fraser, S.J. and Green, A.A., 1987. A software defoliant for geological analysis of band ratios. *International Journal of Remote Sensing,* 8 (3), p.525-532.

Gasmi, A., Gomez, C., Zouari, H., Masse, A., Ducrot, D., 2016. PCA and SVM as geo- computational methods for geological mapping in the southern of Tunisia, using ASTER remote sensing data set. *Arabian Journal of Geoscience,* 9, 753.

Ge, W., Cheng, Q., Tang, Y., Jing, L., and Gao, C., 2018. Lithological Classification Using Sentinel-2A Data in the Shibanjing Ophiolite Complex in Inner Mongolia, China. *Remote Sensing.* 10, 638. DOI: 10.3390/rs10040638.

Harjanto, A., 2010. Alterasi akibat proses hidrothermal di daerah Kulon Progo dan Sekitarnya, Daerah Istimewa Yogyakarta. *Jurnal Ilmu Kebumian Teknologi Mineral,* 23 (3), p.69-81.Haykin, S., 2004. Network, N. A comprehensive foundation. *Neural Network*, 2, 41.

Lehmann, E.L. and Casella, G., 1998. *Theory of Point Estimation, 2nd Edition*, New York: Springer.

Livo, K.E., Clarck, R.N., and Knepper, D.H., 1993. Spectral plot program for accessing the USGS digital spectral library database with MS–DOS personal computers. USGS Open–file. Denver, Colorado, *Report,* 93, 593pp. DOI: 10.3133/ofr93593b

Mondal, A., Kundu, S., Chandniha, S.K., Shukla, R., and Mishra, P. 2012. Comparison of support vector machine and maximum likelihood classification technique using satellite imagery. *Intrnational journal of Remote Sensing GIS 2012,* 1, p.116-123.

Murti, S.H. and Wicaksono, P., 2014. Analisis saluran spektral yang paling berpengaruh dalam identifikasi kesehatan terumbu karang: studi kasus pulau Menjangan Besar dan Menjangan Kecil Kepulauan Karimunjawa. *Majalah Ilmiah Globe,* 16 (2), p.117-224. DOI: 10.14710/marj.v5i4.14435

Nugraha, O.R., 2015. *Geologi dan alterasi hidrotermal di daerah Sangon dan Plampang, Kecamatan Kokap, Kabupaten Kulonprogo, DIY*. Skripsi. Teknik Geologi, Universitas Gadjah Mada. Yogyakarta (*unpublished*). DOI: 10.29408/geodika.v4i2.2643

Pambudi, D., 2017. *Geologi dan mineralisasi logam daerah Sangon, Kokap, Kulon Progo, Yogyakarta*. Skripsi, Universitas Diponegoro, Semarang. DOI: 10.14710/jgt.1.2.2018.74-80

Pramumijoyo, P., 2017. *Geologi, geokimia, dan karakteristik fluida hidrotermal pada endapan epithermal sulfidasi rendah di daerah Sangon, Kokap, DIY.* Tesis. Teknik Geologi, Universitas Gadjah Mada. Yogyakarta (*unpublished*). DOI: 10.29408/geodika.v4i2.2643

Rahardjo, W., Sukandarrumidi, and Rosidi, H.M.D., 1995. *Peta Geologi Lembar Yogyakarta, Jawa*, Pusat Penelitian dan Pengembangan Geologi, Bandung.

Richards, J.A., 1999. *Remote Sensing Digital Image Analysis, An Introduction, 3rd Ed*., Springer-Verlag, Berlin, 363pp.

Ruiz-Armenta, J.R. and Prol-Ledesma, R.M., 1998. Techniques for enhancing the spectral response of hydrothermal alteration minerals in Thematic Mapper images of Central Mexico. *International Journal of Remote Sensing,* 19, p.1981-2000. DOI: 10.1080/014311698215108

Smith, R.B., 2005. Outline of Principle Component Analysis, Site: http://www.yale.edu/ceo/ Documentation/PCA_Outline.pdf. [20 Agustus 2018].

Souza Filho, C.R., and Drury, S.A., 1998. Evaluation of JERS-1 (FUYO-1) OPS and Landsat TM images for mapping of gneissic rocks in arid areas. *International Journal of Remote Sensing,* 19, p.3569-3594.

Sulthoni, J.N., 2017. *Geologi dan kontrol struktur terhadap mineralisasi epithermal berdasarkan analisis tensor dan geokimia di Gunung Ijo dan sekitarnya, Pegunungan Kulonprogo, DIY*. Skripsi. Teknik Geologi, Universitas Jenderal Soedirman. Purwokerto (*unpublished*).

Suroso, Rodhi, A., dan Sutanto, 1986. Usulan Penyesuaian Tata Nama Litostratigrafi Kulon Progo, Daerah Istimewa Yogyakarta, *Proceedings of The 15th Annual Convention of The Indonesian Association of Geologists,* 1, 10pp.

Tangestani, M.H. and Moore, F., 2002. Porphyry copper alteration mapping at the Meiduk area, Iran. *International Journal of Remote Sensing,* 23, p.4815-4826.

Taranik, J.V. and Crósta, A.P., 1996. Remote sensing for geological and mineral resources, an assessment of tools for geoscientists in the future. *International Archives of Photogrammetry and Remote Sensing,* 31 (B7), p.689-698.

Vermote, E.F., El Saleous, N.Z., and Justice, C.O., 2002. Atmospheric Correction of MODIS data in Visible to Middle infrared: First Result. *Remote Sensing of Environment, 83*, p.97-111.

Wang, F., Zhen, Z., Wang, B., and Mi, Z., 2017. Comparative study on KNN and SVM based weather classification models for day ahead short term solar pv power forecasting. *Applied Science,* 8, 28.

Wicaksono, P. and Danoedoro, P., 2012. Multitemporal Vegetation Cover Mapping using ALOS AVNIR-2: The Important of Atmospheric Effect Normalization on Multitemporal Analysis. *Report and Proceedings of ALOS Application and Verification Project in Indonesia. Jakarta*: JAXA dan LAPAN.

Widagdo, A., Pramumijoyo, S., Harijoko, A., and Setiawan, A. 2016. Kajian Pendahuluan Kontrol Struktur Geologi Terhadap Sebaran Batuan-Batuan di Daerah Pegunungan Kulonprogo-Yogyakarta. *Proceedings. Seminar Nasional Kebumian ke-9, 6-7 Oktober. Yogyakarta*, p.9-20.

Yamaguchi, Y. and Naito, C., 2003. Spectral indices for lithologic discrimination and mapping by using the ASTER SWIR bands. *International Journal of Remote Sensing,* 24 (22), p.4311-4323.